



# Inverse estimate of heat flux on a plasma discharge tube to steady-state conditions using thermocouple data and a radiation boundary condition



D. de Faoite<sup>a</sup>, D.J. Browne<sup>a,\*</sup>, J.I. Del Valle Gamboa<sup>b</sup>, K.T. Stanton<sup>a</sup>

<sup>a</sup>School of Mechanical and Materials Engineering, University College Dublin, Ireland

<sup>b</sup>Ad Astra Rocket Company, Liberia, Costa Rica

## ARTICLE INFO

### Article history:

Received 16 January 2014

Received in revised form 28 April 2014

Accepted 28 April 2014

### Keywords:

Inverse problem

Iterative regularisation

Heat flux

Electric propulsion

## ABSTRACT

The heat flux incident upon the inner surface of a plasma discharge tube during a helicon plasma discharge was estimated using an inverse method. Temperature readings were taken from the outer surface of the tube using thermocouples, and the temperature data were interpolated over the tube surface. A numerical inverse procedure based on the Alifanov iterative regularisation method was used to reconstruct the heat flux on the tube inner surface as a function of space and time. In contrast to previously-used inverse models for this application, the current model implements a thermal radiation boundary condition to realistically model the energy exchange in the device. Additionally in these experiments, steady-state operation was reached, and the accurate modelling of the steady-state condition was facilitated by the thermal radiation boundary condition. The variation of heat flux with helicon discharge power, propellant flowrate, and electromagnet current was studied, and it was found that the waste heat flux increased with applied RF power and propellant flowrate, and decreased with current supplied to the electromagnets, over the range of parameter variation tested.

© 2014 Published by Elsevier Ltd.

## 1. Introduction

The Variable Specific-Impulse Magnetoplasma Rocket [1,2] (VASIMR<sup>®</sup>) is an in-space advanced electric propulsion rocket being developed by the Ad Astra Rocket Company (Houston, Texas, USA). It uses strong magnetic fields to contain and direct a high-power plasma for high-specific impulse propulsive thrust. The plasma is created using helicon electromagnetic waves in what is thereby known as the helicon section of the engine [3]. Following ionisation, the plasma is heated to a high temperature by electromagnetic waves at the ion cyclotron resonance frequency (ICRF), significantly increasing the azimuthal velocity of the ions [4]. A magnetic nozzle converts the azimuthal kinetic energy of the ions into axial kinetic energy and facilitates detachment of the plasma from the magnetic field [5]. VASIMR<sup>®</sup> has no electrodes or grid in contact with the plasma, allowing heating of the plasma to very high temperatures and allowing long operational lifetime.

A gas containment tube (GCT), otherwise known as a plasma discharge tube is used in the helicon section of VASIMR<sup>®</sup> to contain the neutral gas prior to ionisation and to ensure physical

separation between the neutral gas and the helicon antenna. The helicon plasma generation process is not completely efficient and results in a significant fraction of the input RF-energy being lost as waste heat. This heat is deposited on the inner surface of the GCT by cross-field particle diffusion and UV radiation [6]. Knowledge of the magnitude and distribution of the waste heat load is essential to designing a suitable thermal management system for the device.

### 1.1. VASIMR<sup>®</sup> VX-CR prototype

In this paper, an investigation of the waste heat flux present on the GCT of the VASIMR<sup>®</sup> VX-CR prototype engine was conducted at the Ad Astra Costa Rica laboratories (Liberia, Costa Rica) [7,8]. The VX-CR consists only of the helicon plasma generation stage of VASIMR<sup>®</sup>, and does not contain an ICRF heating section. Instead, the plasma generated in the helicon stage exhausts into a vacuum chamber. A high-vacuum enclosure upstream of the vacuum chamber, in which the helicon section hardware was located, was constructed from ConFlat<sup>®</sup> (Agilent Technologies, Inc., California, USA) (CF) DN200 (10") hardware. These hardware components provide a high-vacuum seal between the plasma-generation section and the ambient environment. Water lines, RF power supply, thermocouple leads and other diagnostic sensors were connected

\* Corresponding author. Tel.: +353 1716 1901; fax: +353 1283 0534.

E-mail addresses: [daithi.defaoite@ucd.ie](mailto:daithi.defaoite@ucd.ie) (D. de Faoite), [david.browne@ucd.ie](mailto:david.browne@ucd.ie) (D.J. Browne), [juan@adastrarocket.com](mailto:juan@adastrarocket.com) (J.I. Del Valle Gamboa), [kenneth.stanton@ucd.ie](mailto:kenneth.stanton@ucd.ie) (K.T. Stanton).

**Nomenclature**

$e_T$	error between exact and estimated temperatures	$T$	temperature
$e_q$	error between exact and estimated heat fluxes	$T_0$	initial temperature distribution
$I_{\text{mag}}$	electrical current to magnet M1	$Y$	measured temperature
$j$	azimuthal grid node index	$z$	axial coordinate
$J$	objective functional		
$\nabla J$	gradient of objective functional		
$k$	axial grid node index	<b>Greek Symbols</b>	
$L$	axial length of computational domain	$\alpha$	thermal diffusivity
$\dot{m}_g$	propellant gas mass flowrate	$\beta$	search step size
$n$	temporal node index	$\gamma$	iteration index in inverse scheme
$\vec{n}$	outward normal to boundary of computational domain	$\epsilon$	convergence criterion
$N$	number of temporal nodes	$\varepsilon$	emissivity
$N_i$	number of grid nodes in radial direction	$\theta$	azimuthal coordinate
$N_j$	number of grid nodes in azimuthal direction	$\Theta$	sensitivity function
$N_k$	number of grid nodes in axial direction	$\lambda$	thermal conductivity
$P_{\text{RF}}$	RF power to helicon antenna	$A_i$	inner radial surface of computational domain
$q$	heat flux	$A_l$	left axial surface of computational domain
$\tilde{q}$	exact heat flux function	$A_o$	outer radial surface of computational domain
$q^0$	initial heat flux estimate	$A_r$	right axial surface of computational domain
$q_m$	mean heat flux	$\xi$	direction of descent
$q_p$	peak heat flux	$\sigma$	standard deviation
$\Delta q$	heat flux increment	$\sigma_{\text{sb}}$	Stefan–Boltzmann constant
$Q_{\text{tot}}$	total heat load to surface $A_i$	$\tau$	backwards time variable
$r$	radial coordinate	$\psi$	solution of the adjoint problem
$t$	time	$\Omega$	computational domain
$t_f$	final time	$\partial\Omega$	boundary of the computational domain

to the vacuum section via feedthroughs. A schematic representation of the hardware is shown in Fig. 1. Argon propellant was injected through a metal endplate into the GCT. The GCT was made of Type 214 fused quartz (Momentive™ Performance Materials Inc., Quartz Business, Ohio, USA). The helicon RF antenna is located co-axially around the GCT. The plasma flows downstream from the GCT through a ‘choke’—a component that aids in the ionisation of the plasma. An electromagnet, termed magnet M1, is located co-axially with the GCT, encircling the outer surface of the cylindrical vacuum enclosure. The vacuum section wall acts as a thermal barrier between the radiated heat from the GCT outer surface and inner surface of magnet M1. A second electromagnet, termed magnet M2, is located farther downstream, encircling the downstream portion of the choke. These magnets provide the magnetic field required to support helicon waves and also to contain the plasma, once ionised. Both the endplate and choke were water-cooled.

### 1.2. Inverse problems

Inverse analyses are useful to estimate an unknown quantity such as a boundary condition or material property, where direct measurement of that quantity would be difficult or impossible, or where the presence of a physical measurement device would perturb the quantity to be measured [9].

The earliest applications of inverse problems were for the aerospace sector. The number of applications in which inverse analysis has been used has grown greatly in recent years, and inverse problems are now found in virtually every branch of science and engineering [9]. Inverse analysis is used extensively to estimate various different quantities in heat transfer problems: for the estimation of boundary conditions, rates of internal heat generation (e.g. [10,11]), and thermophysical properties (e.g. [12]). Such problems are referred to as inverse heat transfer problems (IHTP).

In the current application plasma generated in the helicon section of the VASIMR® VX-CR prototype causes a heat flux of

unknown magnitude and spatial distribution on the inner surface of the GCT (surface  $A_i$ , see Fig. 2). Direct measurement of this heat flux  $q(A_i, t)$ , or of the temperature on the inner surface of the GCT would be difficult, due to the presence of the plasma and the RF field created by the helicon antenna.

In the current application, temperature data are available from thermocouple measurements for the outer surface of the GCT (surface  $A_o$ , see Fig. 2). The boundary conditions at the left and right surfaces of the tube (surfaces  $A_l$  and  $A_r$ , see Fig. 2), the initial condition, and the thermo-physical properties of the GCT are also known. Reconstruction of the heat flux  $q(A_i, t)$  on the inner surface of the GCT (surface  $A_i$ ) using the known thermo-physical properties, problem geometry, initial condition, known boundary conditions for surfaces other than surface  $A_i$ , and measured temperature data  $Y(A_o, t)$ , is an example of an inverse problem.

### 1.3. Inverse solution methods

Numerous methods have been developed to mathematically treat inverse problems. These include Tikhonov Regularisation [13], the Levenberg–Marquardt method [14,15], the Beck Sequential Function Specification method [16,17], and the Alifanov iterative regularisation method [18,19]. Özisik and Orlande [9] provide a more complete classification of the various solution techniques.

The inverse solution method used in this work is the iterative regularisation method of Alifanov. This technique is one of the most universally applicable and widely used inverse solution techniques. The method is computationally efficient, can yield accurate results, does not require any *a priori* information about the form of the function sought [20], and can be used for the solution of both linear and non-linear problems [19]. Use of this technique for the solution of 3-D boundary inverse heat conduction problems is well documented in the literature (e.g. [21–25]). The Alifanov iterative

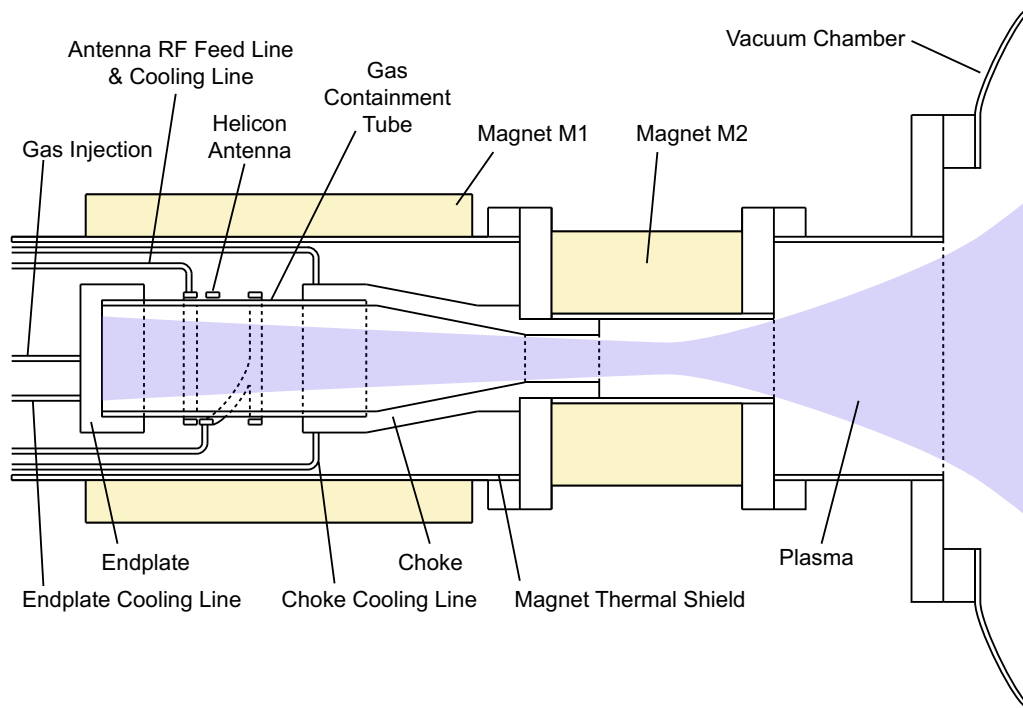


Fig. 1. Schematic representation of VASIMR® VX-CR prototype engine.

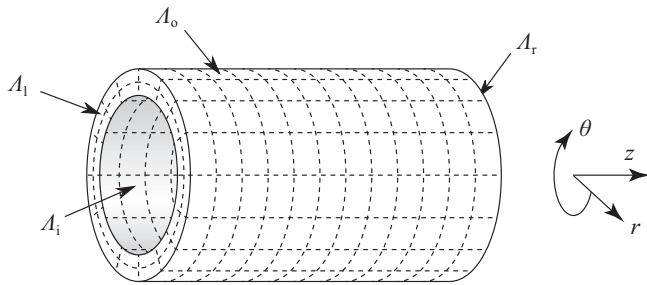


Fig. 2. Schematic representation of spatial domain  $\Omega$  for the inverse problem calculation. Grid divisions are schematic only, and do not represent actual locations.

regularisation method is described in Section 1.4 in the context of this application.

#### 1.4. Alifanov iterative regularisation method

The Alifanov method was used to estimate the heat flux on the inner surface of the GCT using temperature measurement data from the outer surface of the GCT. Alifanov's solution methodology is composed of the following different steps. The first step in the solution methodology is to re-state the inverse problem as an extremal statement [18]. This extremal formulation is used as an optimisation criterion. In effect, the inverse problem is reduced to a general optimisation problem. An arbitrarily-chosen initial estimate of heat flux is assumed for the inner surface of the GCT. Using this, the direct problem is solved, leading to a calculation for the temperature field in the tube and for the tube outer surface. The difference (error) between the calculated temperature response for surface  $A_o$  and the measured temperatures is characterised by a temperature residual functional.

The estimate of the heat flux on the inner surface of the tube is appropriately adjusted to reduce the error between the measured and computed temperatures and thereby find a near-optimal solution. This process is performed iteratively using gradient

descent methods. Gradient descent methods commonly used for the Alifanov solution method include the steepest descent method (SDM) and conjugate gradient method (CGM). In this work the SDM is used as it is simple to implement, although faster convergence can be achieved by use of the CGM.

The stability of the solution technique is achieved by stopping the iterative optimisation process when the residual functional is smaller than some quantity  $\epsilon$ . This method of ensuring solution stability is referred to as *iterative regularisation* [26].

Calculation of an appropriate adjustment to the heat flux estimate requires the creation and solution of two ancillary problems, termed the adjoint and sensitivity problems, described later.

## 2. Direct problem

### 2.1. Computational domain

The spatial domain for this problem is that of a cylindrical conducting medium, corresponding to an axial section of the GCT, of length 100 mm, inner radius 47.5 mm, and outer radius 50.0 mm. A cylindrical coordinate system is used. The spatial domain, illustrated in Fig. 2, is denoted  $\Omega(r, \theta, z)$ . By convention used in this work, plasma flow is from axial left to axial right locations, so that  $A_l$  and  $A_r$  correspond respectively to plasma flow upstream and downstream locations. The boundary of the conducting medium is  $\partial\Omega$ , which for this application is given by  $\partial\Omega \equiv A_i \cup A_l \cup A_o \cup A_r$ .

As discussed in Section 2.3, the conducting medium is assumed to be composed of an isotropic, homogeneous solid, with properties (density, thermal conductivity, isobaric specific heat capacity) that are independent of temperature. Furthermore, the surfaces of the conducting medium are assumed to be diffuse grey surfaces, and the material itself is assumed to be opaque.

### 2.2. Initial and boundary conditions

The temperature of surface  $A_o$  is known for all times from thermocouple measurements. Direct temperature measurements are

not available from surface  $A_i$ . It is assumed that at the initial time ( $t = 0$ ), the temperature at a point in the computational domain of any radial position is equal to the measured outer surface temperature at the same azimuthal and axial position. The initial temperature field is denoted  $T_0(r, \theta, z)$ .

The temperature of the left and right surfaces,  $A_l$  and  $A_r$  respectively, are not measured and are unknown. A homogeneous Neumann (insulated) boundary condition is used for these surfaces. Due to the low cross-sectional area of these surfaces and the low thermal conductivity of fused quartz, the magnitude of heat flux conducted axially through these boundary surfaces is small compared to the magnitude of heat flux radiated from surface  $A_o$ .

In performing an inverse heat transfer analysis for experiments conducted on the GCT of the VASIMR<sup>®</sup> VX-50 prototype engine, Mulcahy et al. [25] used a homogeneous Neumann (insulated) boundary condition for the outer surface of the computational domain. This approach is suitable where the outer surface temperature is sufficiently low that radiation heat transfer is negligible. However, at high temperatures, where radiation heat transfer becomes significant, the approach of Mulcahy et al. becomes insufficient.

During several of the current experiments the maximum temperature of surface  $A_o$  exceeded 400 °C, resulting in significant thermal radiation heat transfer between the outer surface of the GCT and the inner surface of the magnet thermal shield. A boundary condition that models this radiation heat flux is therefore required. In this work, the following approach is taken. The emissivity of Type 214 fused quartz was assumed to be  $\approx 0.75$  [27], and the emissivity of the stainless steel thermal jacket was assumed to be  $\approx 0.60$ . The temperature of the thermal jacket was 15 °C. The outer surface of the GCT has a line-of-sight only to the thermal shield, antenna, endplate, choke, and alumina rods used for thermocouple lead mounting. The antenna, endplate and choke are water-cooled, and did not rise significantly above ambient temperature. The electro-magnets encircling the thermal jacket were also water-cooled. The effect of the antenna or the alumina rods on the radiation view factors is not modelled. All surfaces visible to  $A_o$  are assumed to be at a uniform temperature equal to that of the thermal jacket inner surface. The radiation view factor of the surface  $A_o$  to the thermal jacket and surrounding hardware is 1.0, as it is fully enclosed. Given the known temperature of the surface  $A_o$ , the net radiation heat flux from surface  $A_o$  may therefore easily be calculated using standard radiation heat transfer equations.

The GCT and thermal jacket may be modelled approximately as two long concentric cylinders. For infinitely long concentric cylinders exchanging radiation, where the facing surfaces are diffuse grey, the net radiation heat flux from the inner cylinder (cylinder 1) to the outer cylinder (cylinder 2) is [28]:

$$q_{12} = \frac{\sigma_{\text{sb}}(T_1^4 - T_2^4)}{\frac{1}{\varepsilon_1} + \frac{1-\varepsilon_2}{\varepsilon_2} \left(\frac{r_1}{r_2}\right)} \quad (1)$$

where  $\sigma_{\text{sb}}$  is the Stefan–Boltzmann constant,  $T_1$  and  $\varepsilon_1$  are the temperature and emissivity of the outer surface of the inner cylinder,  $T_2$  and  $\varepsilon_2$  are the temperature and emissivity of the inner surface of the outer cylinder, and  $r_1$  and  $r_2$  are respectively the radii of the inner and outer cylinders. From Fourier's law of heat conduction, the outward normal temperature gradient of the inner cylinder is then given by:

$$\frac{\partial T}{\partial \vec{n}} = \frac{-\sigma_{\text{sb}}(T_1^4 - T_2^4)}{\lambda_1 \left(\frac{1}{\varepsilon_1} + \frac{1-\varepsilon_2}{\varepsilon_2} \left(\frac{r_1}{r_2}\right)\right)} \quad (2)$$

where  $\lambda_1$  is the thermal conductivity of the inner cylinder. As the outward normal temperature gradient of the GCT may be

calculated, the radiation heat transfer from surface  $A_o$  can therefore be modelled using a non-homogeneous Neumann boundary condition. This significantly simplifies the inverse problem form, as radiation boundary conditions do not have to be derived for the adjoint and sensitivity problems.

A similar approach was taken by Lefèvre and Le Niliot who performed an inverse heat transfer analysis on rectangular concrete bars using the boundary element method (BEM) [29,30]. In their experiments, temperature measurements were taken from the outer surface of the bars using a thermographic camera. The outer surface of the bars were painted with a black paint of known emissivity. The radiation and convection ambient temperature were also known. Lefèvre and Le Niliot used the surface temperature measurements to calculate the surface heat flux, using radiation theory for the radiative component, and using a heat transfer coefficient correlation for the convective component.

The boundary condition used in this work for the outer surface of the GCT contrasts to that used by Mulcahy et al. [25], where an insulated boundary condition was used. Due to the higher temperatures reached in the current experiments the radiation boundary condition is required to realistically model the energy exchange in the device. At the temperatures reached in the current experiments there is a significant difference between the waste heat flux predicted with the current model and that predicted when using an insulated boundary condition. This modification is a natural progression of model development from that of Mulcahy et al.

### 2.3. Material properties

The material properties are modelled as being temperature independent. Modelling of material properties that are functions of temperature would result in a non-linear problem, making the inverse analysis significantly more complicated. Where the variation in material properties is small, it is reasonable to use temperature-averaged property values.

The temperature of the GCT spanned from 10 °C to a maximum of 430 °C during the current experiments. Temperature-averaged values of thermal diffusivity and effective thermal conductivity were calculated for this temperature range based on published property data [31,32]. The effective thermal conductivity rather than the true thermal conductivity was used, as radiation heat transfer becomes an important heat transfer mechanism in translucent media above  $\approx 300$  °C. The calculated temperature-averaged thermal diffusivity was  $783 \times 10^{-9} \text{ m}^2 \text{ s}^{-1}$ , and the temperature-averaged effective thermal conductivity was  $1.62 \text{ W m}^{-1} \text{ K}^{-1}$ . The variation in thermal diffusivity and conductivity over this temperature range is reasonably small.

### 2.4. Statement of the direct problem

Implementing the initial and boundary conditions discussed in Section 2.2, the direct heat conduction problem may be stated as:

$$\left[ \frac{\partial^2 T(\Omega, t)}{\partial r^2} + \frac{1}{r} \frac{\partial T(\Omega, t)}{\partial r} + \frac{1}{r^2} \frac{\partial^2 T(\Omega, t)}{\partial \theta^2} + \frac{\partial^2 T(\Omega, t)}{\partial z^2} \right] = \frac{1}{\alpha} \frac{\partial T(\Omega, t)}{\partial t} \quad \text{in } (\Omega, t) \quad (3a)$$

$$-\lambda \frac{\partial T(A_i, t)}{\partial \vec{n}} = q(A_i, t), \quad \Omega = A_i, \quad t > 0 \quad (3b)$$

$$-\lambda \frac{\partial T(A_o, t)}{\partial \vec{n}} = q(A_o, t), \quad \Omega = A_o, \quad t > 0 \quad (3c)$$

$$-\lambda \frac{\partial T(A_l, t)}{\partial \vec{n}} = 0, \quad \Omega = A_l, \quad t > 0 \quad (3d)$$

$$-\lambda \frac{\partial T(A_r, t)}{\partial \vec{n}} = 0, \quad \Omega = A_r, \quad t > 0 \tag{3e}$$

$$T(\Omega, 0) = T_0(\Omega), \quad \forall \Omega, \quad t = 0 \tag{3f}$$

where  $T_0$  is the initial temperature distribution,  $\partial/\partial \vec{n}$  is the derivative along the outward normal to the surface of the computational domain  $\partial\Omega$ ,  $\alpha$  is the thermal diffusivity, and  $q(A_o, t)$ , the net heat flux into surface  $A_o$  is assumed to be known;  $q(A_o, t)$  is calculated from measured temperatures from surface  $A_o$ .

### 3. Inverse problem

The quantity to be recovered is denoted  $q(A_i, t)$ . The measured temperature of surface  $A_o$  is denoted  $Y(A_o, t)$ , which in general contains measurement errors. The solution to the direct problem is denoted  $T(\Omega, t; q)$ , calculated using a given (estimated) value of  $q(A_i, t)$ . The inverse problem can be stated as follows [20,18]: find  $q(A_i, t)$  such that:

$$T(A_o, t; q) \approx Y(A_o, t) \quad \text{for } 0 \leq t \leq t_f \tag{4}$$

where  $t_f$  is the final time. Due to errors in the model and measurement errors, the above equation must be solved in terms of least squares [20].

#### 3.1. Residual functional

As described in Section 1.4, the first step in the solution methodology is to re-state the inverse problem as an extremal statement [18]. The extremal statement has the form of a temperature residual functional, denoted  $J$ . The  $L_2$  norm (mean-square residual) is typically used as the measure of deviation (or proximity) between the computed and measured temperatures (i.e. between functions  $T$  and  $Y$ ) [18]:

$$J^\gamma(q^\gamma(A_i, t)) = \int_t \int_{A_o} [T^\gamma(A_o, t; q^\gamma) - Y(A_o, t)]^2 d\Omega dt \tag{5}$$

$T^\gamma(A_o, t; q^\gamma)$  is the computed temperature field on surface  $A_o$  at iteration  $\gamma$  for the heat flux estimate  $q^\gamma(A_i, t)$  at iteration  $\gamma$ . The functional is evaluated once in every iteration of the inverse problem, denoted  $J^\gamma(q^\gamma(A_i, t))$ .

### 4. Steepest descent method for minimisation

The estimation of the sought quantity  $q(A_i, t)$  is obtained by the iterative minimisation of the residual functional over successive iterations [18]. The minimisation of  $J(q(A_i, t))$  leads to a calculated temperature field that closely matches the measured temperature field.

To minimise the functional  $J(q(A_i, t))$ , and thus approach a solution, a discrete iterative process is used. An arbitrarily-chosen initial estimate is made of the heat flux, from which an estimate of the temperature field in  $\Omega$  is calculated using the direct model. The residual functional is then calculated to quantify the deviation between numerically calculated and experimentally determined temperature fields. The functional is minimised by the iterative re-calculation of the heat flux  $q(A_i, t)$  based on the following iteration scheme:

$$q^{\gamma+1}(A_i, t) = q^\gamma(A_i, t) - \beta^\gamma \xi^\gamma(A_i, t), \quad \gamma = 0, 1, \dots \tag{6}$$

with  $q^0(A_i, t)$  being the initial guess of  $q(A_i, t)$ . At each iteration the heat flux is incremented by the quantity  $\beta^\gamma \xi^\gamma(A_i, t)$ , where  $\beta^\gamma$  is the search step size from iteration  $\gamma$  to  $\gamma + 1$  and  $\xi^\gamma(A_i, t)$  is the direction of descent (search direction) at iteration  $\gamma$ . The direction of descent is given by the gradient of the functional with respect to changes in heat flux  $q(A_i, t)$ :

$$\xi^\gamma(A_i, t) = \nabla J^\gamma(q^\gamma(A_i, t)) \tag{7}$$

#### 4.1. Adjoint problem

In order to use gradient methods of minimisation the functional gradient  $\nabla J(q(A_i, t))$  with respect to changes in  $q(A_i, t)$  needs to be calculated at every iteration. The inverse solution method of Alifanov employs a computationally efficient method of calculating the functional gradient, called the *adjoint equation method* [20]. This requires the construction and solution of what is called the *adjoint problem*. The gradient of the functional is then computed from the solution of the adjoint problem for surface  $A_i$  [20,18].

Construction of the adjoint problem is described in the literature [20,18,19]. For the application described in this work, the adjoint function  $\psi(\Omega, t)$  is the solution of the following problem:

$$\left[ \frac{\partial^2 \psi(\Omega, t)}{\partial r^2} + \frac{1}{r} \frac{\partial \psi(\Omega, t)}{\partial r} + \frac{1}{r^2} \frac{\partial^2 \psi(\Omega, t)}{\partial \theta^2} + \frac{\partial^2 \psi(\Omega, t)}{\partial z^2} \right] = -\frac{1}{\alpha} \frac{\partial \psi(\Omega, t)}{\partial t} \quad \text{in } (\Omega, t) \tag{8a}$$

$$-\lambda \frac{\partial \psi(A_i, t)}{\partial \vec{n}} = 0, \quad \Omega = A_i, \quad t > 0 \tag{8b}$$

$$-\lambda \frac{\partial \psi(A_o, t)}{\partial \vec{n}} = T(A_o, t; q) - Y(A_o, t), \quad \Omega = A_o, \quad t > 0 \tag{8c}$$

$$-\lambda \frac{\partial \psi(A_r, t)}{\partial \vec{n}} = 0, \quad \Omega = A_r, \quad t > 0 \tag{8d}$$

$$-\lambda \frac{\partial \psi(A_i, t)}{\partial \vec{n}} = 0, \quad \Omega = A_i, \quad t > 0 \tag{8e}$$

$$\psi(\Omega, t) = 0, \quad \forall \Omega, \quad t = t_f \tag{8f}$$

The adjoint problem has no initial condition but has a final condition. A new time variable  $\tau = t_f - t$  is introduced. This changes the adjoint problem into the form of the direct problem, making it solvable by the same method [18].

#### 4.2. Sensitivity problem

At each iteration the step size  $\beta^\gamma$  is chosen such that it minimises  $J^{\gamma+1}(q^{\gamma+1}(A_i, t))$  along the direction of descent,  $\xi^\gamma$ :

$$\beta^\gamma = \underset{\beta^\gamma}{\text{argmin}} J^{\gamma+1}(q^\gamma - \beta^\gamma \nabla J^\gamma), \quad \beta^\gamma > 0 \tag{9}$$

An expression for the functional value  $J^{\gamma+1}(q^{\gamma+1}(A_i, t))$  in the search direction as a function of step size  $\beta^\gamma$  is thus required. This is achieved by the construction and solution of a *sensitivity problem*, the solution of which yields the directional derivatives of the temperature field in the direction of descent.

To construct the sensitivity problem the direct problem is written first in terms of  $q$  and then for a perturbed heat flux ( $q + \Delta q$ ). The solution of the direct problem for heat flux  $q$  is  $T(\Omega, t; q)$ , and for the perturbed heat flux the solution is  $T(\Omega, t; q + \Delta q)$ . Subtracting the resulting expressions for the direct heat problem, and neglecting second-order terms yields the sensitivity problem in terms of the sensitivity function  $\Theta(\Omega, t)$ :

$$\left[ \frac{\partial^2 \Theta(\Omega, t)}{\partial r^2} + \frac{1}{r} \frac{\partial \Theta(\Omega, t)}{\partial r} + \frac{1}{r^2} \frac{\partial^2 \Theta(\Omega, t)}{\partial \theta^2} + \frac{\partial^2 \Theta(\Omega, t)}{\partial z^2} \right] = \frac{1}{\alpha} \frac{\partial \Theta(\Omega, t)}{\partial t} \quad \text{in } (\Omega, t) \tag{10a}$$

$$-\lambda \frac{\partial \Theta(A_i, t)}{\partial \vec{n}} = \Delta q(A_i, t), \quad \Omega = A_i, \quad t > 0 \tag{10b}$$

$$-\lambda \frac{\partial \Theta(A_o, t)}{\partial \vec{n}} = 0, \quad \Omega = A_o, \quad t > 0 \tag{10c}$$

$$-\lambda \frac{\partial \Theta(A_l, t)}{\partial \vec{n}} = 0, \quad \Omega = A_l, \quad t > 0 \quad (10d)$$

$$-\lambda \frac{\partial \Theta(A_r, t)}{\partial \vec{n}} = 0, \quad \Omega = A_r, \quad t > 0 \quad (10e)$$

$$\Theta(\Omega, t) = 0, \quad \forall \Omega, \quad t = 0 \quad (10f)$$

The perturbation of heat flux used in the sensitivity problem is the descent direction  $\xi^y$ . That is, the directional derivatives  $\Theta(\Omega, t; \Delta q)$  that are calculated are the directional derivatives in the direction of descent.

### 4.3. Step size

The temperature field  $T^{\gamma+1}(\Omega, t; q^{\gamma+1})$  at iteration  $\gamma + 1$  may be approximated by using a truncated Taylor series expansion, taking the first two terms [22]:

$$T^{\gamma+1}(\Omega, t; q^{\gamma+1}) \approx T^{\gamma}(\Omega, t; q^{\gamma}) - \beta^{\gamma} \Theta^{\gamma}(\Omega, t; \Delta q^{\gamma}) \quad (11)$$

Writing Eq. (11) for surface  $A_o$  and substituting into Eq. (5) yields an expression for the functional at iteration  $\gamma + 1$ :

$$J^{\gamma+1}(q^{\gamma+1}(A_o, t)) = \int_t \int_{A_o} [T^{\gamma}(A_o, t; q^{\gamma}) - \beta^{\gamma} \Theta^{\gamma}(A_o, t; \Delta q^{\gamma}) - Y(A_o, t)]^2 dA_o dt \quad (12)$$

Minimising with respect to  $\beta^{\gamma}$ , an expression for the step size that minimises the functional value in the search direction at iteration  $\gamma + 1$  then results:

$$\beta^{\gamma} = \frac{\int_t \int_{A_o} [\Theta^{\gamma}(A_o, t)] [T^{\gamma}(A_o, t; q^{\gamma}) - Y(A_o, t)] dA_o dt}{\int_t \int_{A_o} [\Theta^{\gamma}(A_o, t)]^2 dA_o dt} \quad (13)$$

### 4.4. Stopping criterion

As iterations progress, the calculated estimate of the sought quantity (heat flux) initially improves, but can deteriorate with further iterations. A stopping criterion is thus required to stop the iteration scheme at an appropriate point [18]. The discrepancy principle has been found by many authors (e.g. [23,33,34]) to be an appropriate stopping criterion. Iterations are stopped when the functional value falls below the value of  $\epsilon$ :

$$\epsilon = \int_t \int_{A_o} \sigma^2 dA_o dt \quad (14)$$

where  $\sigma$  is the standard deviation of the temperature measurements.

In order to quantify the random component of the measurement error, the thermocouple signals were digitally filtered. The standard deviation for the thermocouple signals, based on the difference between the smoothed (filtered) and un-smoothed readings, was then calculated. The calculated standard deviation for all experiments was found to be very small.

Another source of error is introduced in the interpolation of thermocouple readings to the finite difference grid. For this process, the standard deviation was again calculated, based on the difference in temperature between the true thermocouple readings and the temperatures in the finite difference grid at locations corresponding to the thermocouple locations. The errors introduced in this interpolation were found to be significantly larger than the random error in thermocouple readings. These calculated values of standard deviation were therefore used as the basis of the stopping criterion, according the discrepancy principle.

## 5. Computational procedure

A flowchart depicting steps required for the solution of the inverse problem using the Alifanov solution method is shown in Fig. 3.

The Alifanov inverse solution method involves the solution of three different problems that have similar forms. These are the direct problem, the adjoint problem, and the sensitivity problem. These problems can be configured to be solved by the same numerical method. In this work, the finite difference method (FDM) with a forward Euler time-marching scheme was used to solve the PDE models, as this technique is simple to implement.

The number of azimuthal, axial and radial nodes to use for the computational grid must be given some consideration. A higher number of nodes in principle allows finer representation of spatial variations in temperature. However, as the number of thermocouple readings is finite, increasing the number of nodes only improves the temperature estimate up to a limit. Using more spatial nodes also leads to a smaller required timestep size for stability in the explicit finite difference scheme, leading to a longer solution time. 16 Grid divisions in the azimuthal direction, 21 in the axial direction and 7 in the radial direction were used. For the number of thermocouples used this number of nodes leads to only a small error in temperature estimation compared to using an arbitrarily high number of nodes, providing a balance between introduced temperature error and computational time requirement.

## 6. Verification

A series of numerical simulations were carried out to verify the inverse heat transfer method. The same computational domain, boundary conditions and material properties were used for the

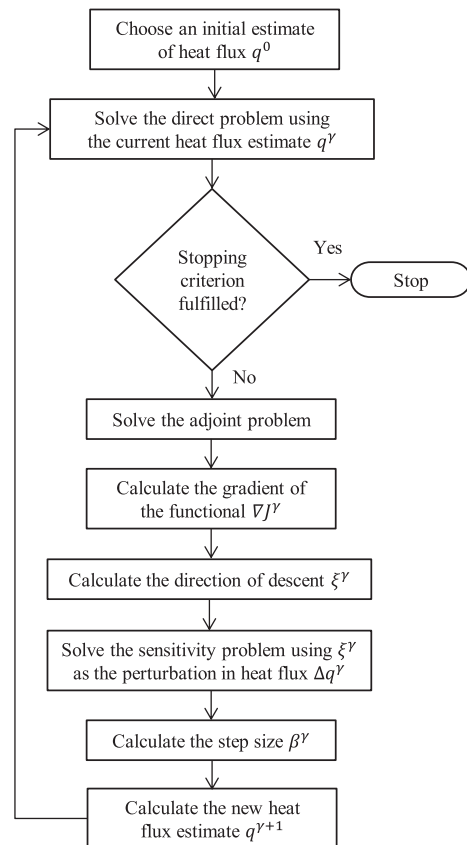


Fig. 3. Flowchart describing solution algorithm for the Alifanov method.

verification studies as for the experimental studies, as described in Sections 2.1–2.3.

Simulated transient temperature data were generated by solving the direct heat transfer problem for a known heat flux applied to surface  $A_i$ . Solution of the direct heat transfer problem yields the exact temperature response of surface  $A_o$ . Normally-distributed artificial noise was added to the calculated temperature response of surface  $A_o$  to simulate temperature measurements containing random measurement error. The added noise had a mean of 0 K and a standard deviation of 5 K. These simulated temperature measurements were then used as an input to the inverse model. Iterative solution of the inverse model yielded an estimate of the heat flux applied to surface  $A_i$  and the temperature field in domain  $\Omega$ . The true and estimated heat fluxes and temperature fields were then compared to assess the adequacy of the inverse model.

The simulated heat flux applied to surface  $A_i$  varied both spatially and temporally. Two different functions were used, the first having a ‘step’ and the second having a ‘ramp’ temporal dependence of heat flux. Both simulations were run for 1200 s, with zero applied heat flux for the first 200 s and last 200 s of each experiment. A peak heat flux value of  $1 \times 10^4 \text{ W m}^{-2}$  was used for both cases. For the ‘step’ temporal variation the heat flux is given by:

$$\tilde{q}(\theta, z, t) = \left( -2\left(\frac{z}{L}\right)^2 + 2\left(\frac{z}{L}\right) + \frac{1}{2} \right) \left( \frac{4 + \cos 2\theta}{5} \right) (1 \times 10^4) \quad \text{for } 200 \leq t \leq 1000 \quad (15a)$$

$$\tilde{q}(\theta, z, t) = 0 \quad \text{for } t < 200, t > 1000 \quad (15b)$$

And for the ‘ramp’ temporal variation the heat flux is given by:

$$\tilde{q}(\theta, z, t) = \left( -2\left(\frac{z}{L}\right)^2 + 2\left(\frac{z}{L}\right) + \frac{1}{2} \right) \left( \frac{4 + \cos 2\theta}{5} \right) (12.5(t - 200)) \quad \text{for } 200 \leq t \leq 1000 \quad (16a)$$

$$\tilde{q}(\theta, z, t) = 0 \quad \text{for } t < 200, t > 1000 \quad (16b)$$

Here  $\theta$  is the azimuthal coordinate and  $z$  is the axial coordinate. The value of  $z$  ranges from 0 at the upstream edge of the computational domain, to  $L$ , the axial length of the computational domain (0.1 m). The spatial variation of heat flux normalised to a peak heat flux of  $1 \text{ W m}^{-2}$  is plotted in Fig. 4. This spatial variation of heat flux is a slightly modified version of that used by Mulcahy et al. [25].

The simulations were run until the problem reached the stopping condition dictated by the discrepancy principle, based on the standard deviation of the added temperature noise. The functional value monotonically decreased with increasing iteration number.

Three locations on the tube outer surface were selected for evaluation of the temperature and heat flux estimates: point ‘A’:

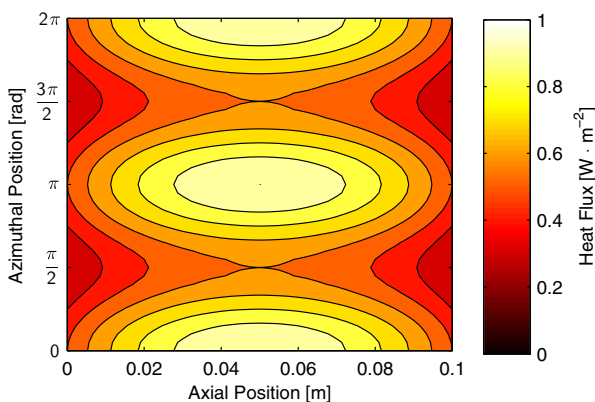


Fig. 4. Normalised heat flux spatial distribution for inverse method verification.

$\theta = 0 \text{ rad}$ ,  $z = 50 \text{ mm}$ , point ‘B’:  $\theta = \pi/4 \text{ rad}$ ,  $z = 30 \text{ mm}$ , point ‘C’:  $\theta = \pi/2 \text{ rad}$ ,  $z = 10 \text{ mm}$ . The true temperature and the temperature calculated by solution of the inverse problem on the tube outer surface, along with the true heat flux and heat flux calculated by the solution of the inverse problem on the tube inner surface, are plotted in Figs. 5 and 6.

### 6.1. Quantification of error

Two metrics were used to gauge how well the temperature and heat flux estimates matched the true values. The deviation between the exact temperature (with added noise) and the calculated temperature at every grid node on  $A_o$  is computed as:

$$e_T = \frac{1}{N_n N_j N_k} \sum_{n=1}^{N_n} \sum_{j=1}^{N_j} \sum_{k=1}^{N_k} \sqrt{\frac{(T_{j,k}^n - Y_{j,k}^n)^2}{(Y_{j,k}^n)^2}} \times 100 \quad (17)$$

Here  $T_{j,k}^n$  and  $Y_{j,k}^n$  are the discretised temperature from the solution of the inverse problem and the discretised exact temperature, respectively, for each grid node on surface  $A_o$ . The subscripts  $j$  and  $k$  are the azimuthal and axial grid node indices respectively, and the superscript  $n$  is the index of discretised time.  $N_n$ ,  $N_j$  and  $N_k$  are the number of temporal, azimuthal and axial nodes respectively, so that the product  $N_n N_j N_k$  is the total number of points at which temperatures (or heat fluxes) are compared.

The deviation between the exact and the calculated heat flux profiles at every grid node on  $A_i$  is computed as:

$$e_q = \sqrt{\frac{1}{N_n N_j N_k} \sum_{n=1}^{N_n} \sum_{j=1}^{N_j} \sum_{k=1}^{N_k} (q_{j,k}^n - \tilde{q}_{j,k}^n)^2} \quad (18)$$

Here  $\tilde{q}_{j,k}^n$  and  $q_{j,k}^n$  are the discretised true heat flux and the discretised estimate of heat flux from the solution of the inverse problem, respectively, for each grid node on surface  $A_i$ . An error metric of the form of Eq. (17) would be unsuitable for the heat flux, as the applied heat flux is zero for periods  $t < 200 \text{ s}$  and  $t > 1000 \text{ s}$ , which would result in the denominator of such a metric being zero for the corresponding discretised times.

The temperature and heat flux error metrics are calculated by assuming that each spatial grid node on surface  $A_o$  corresponds to one ‘measurement’ location, rather than comparing temperatures and heat fluxes at the actual thermocouple locations. The error metrics  $e_T$  and  $e_q$  therefore exclude the type of error that is introduced with the experimental measurements due to spatial mapping of discrete temperature measurements.

### 6.2. Verification results

For the verification tests the total errors in temperature and heat flux estimates are given in Table 1. The error in temperature estimation in both cases is small, while the error in heat flux is non-trivial. For both cases the error in temperature estimation are comparable. This is to be expected, as iterations are continued until the stopping criterion—a measure of the error in temperature estimation—is reached. The error in heat flux estimation is a limitation of the inverse method, resulting from the ill-posed nature of the problem.

The error in temperature and heat flux estimates is greatest at times when sharp changes in heat flux magnitude occur (at 200 s and 1000 s). For the verification tests in the current work, noise with a relatively high standard deviation of 5 K has been added. The verification results illustrate that this inverse method can stably solve the inverse problem for the current these boundary

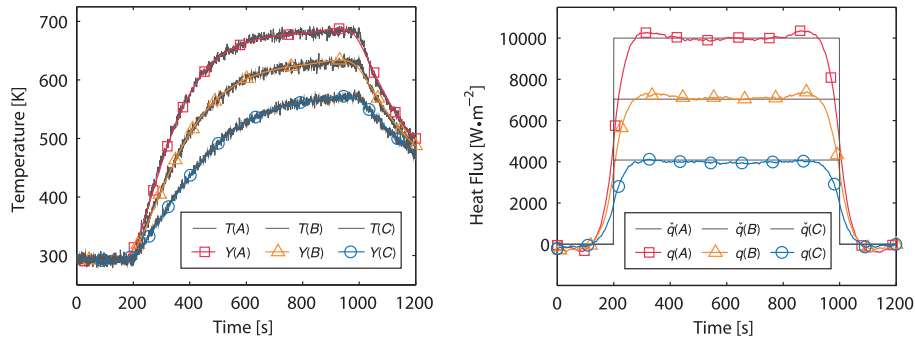


Fig. 5. The exact and estimated temperatures (left), and exact and estimated heat fluxes (right), at points ‘A’, ‘B’ and ‘C’ for the ‘step’ heat flux case.

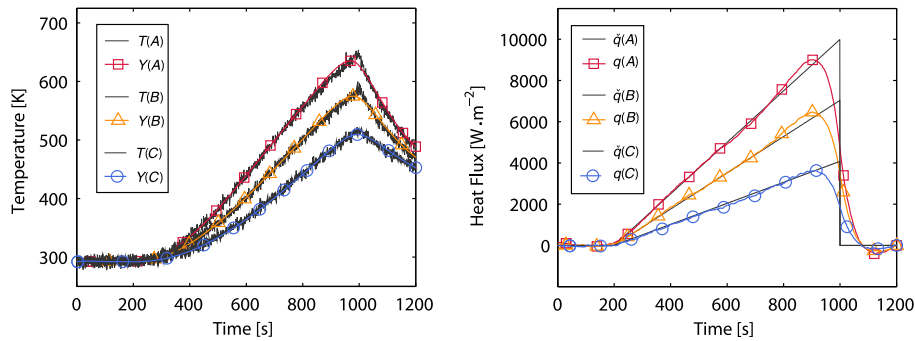


Fig. 6. The exact and estimated temperatures (left), and exact and estimated heat fluxes (right), at points ‘A’, ‘B’ and ‘C’ for the ‘ramp’ heat flux case.

Table 1

Error between exact and estimated temperatures ( $e_T$ ) and error between exact and estimated heat fluxes ( $e_q$ ) for different heat flux inputs.

Heat Flux Input	$e_T$ (%)	$e_q$ ( $W\ m^{-2}$ )
Step	0.988	778
Ramp	1.133	585

Table 2

Set-points for VASIMR® VX-CR thermal experiments.

Input setting	Magnet current (A)	RF power (W)	Gas flowrate ( $mg\ s^{-1}$ )
Low	800	800	2.77
Centre	1000	1100	-
High	1200	1400	8.31

conditions, in the presence of measurement error, with reasonable accuracy.

## 7. Experimental procedure

A series of experiments were conducted on the VASIMR® VX-CR engine in order to investigate the effects of varying the input parameters on the magnitude and distribution of the waste heat flux. The high heat flux from the plasma, in addition to the low thermal conductivity of the fused quartz GCT results in the GCT reaching high temperatures.

### 7.1. Variation of controllable parameters

In order to investigate the effect on waste heat flux when certain controllable parameters are varied, a design of experiments (DOE) analysis was conducted. Three controlled parameters were varied: the electrical current supplied to magnet M1, the injection mass flowrate of propellant, and the RF power supplied to the helicon antenna. The electrical current to magnet M2 was kept constant for all experiments. Three experimental set-points were used for the magnet current and RF power, while two set-points were used for the gas flowrate. The experimental set-points are given in Table 2. The DOE permutation led to 18 experiments.

### 7.2. Thermocouple measurements

Temperature measurements were taken at several discrete locations on the outer surface of the GCT using thermocouples. Thermocouples cannot be located on the inner surface of the GCT without perturbing the plasma generation process. The thermocouples were bonded to the tube surface using a commercially supplied, alumina-based ceramic adhesive (Cotronics Corp. (New York, USA) Resbond™ 940HT). Capacitors were connected in parallel to each set of thermocouple leads to reduce the RF currents induced in the thermocouples by the RF antenna.

In total, 22 type-K thermocouples were attached to the GCT. Three axial lines of five thermocouples each were used, azimuthally spaced  $2\pi/3$  rad from each other. An additional three thermocouples were located between the two helicon straps. Two further thermocouples were located at each end of the GCT in the ceramic binder between the surface of the GCT and endplate, and GCT and choke. As the spatial density of thermocouple measurements was greatest in the central portion of the tube, a section of the GCT only 100 mm in length was used as the computational domain for the inverse analysis. The thermocouples attached to the central portion of the GCT are shown schematically in Fig. 7.

The nominal sampling frequency for the thermocouples was 1 Hz. Digitization and recording of thermocouple signals was achieved with a National Instruments (Austin, Texas, USA) LabVIEW™ data acquisition (DAQ) system.

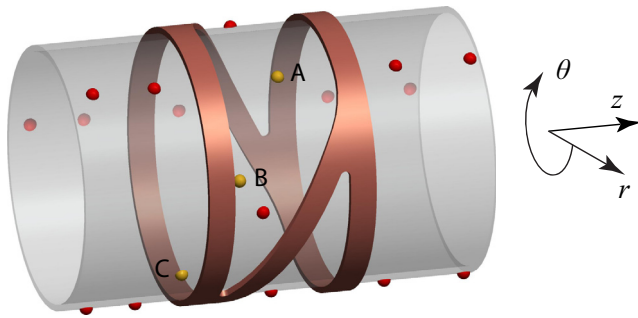


**Fig. 7.** Schematic representation of thermocouple locations on the central portion of GCT. Red dots represent thermocouple locations (light red dots indicate the position of thermocouples on the obscured side of the tube). Yellow dots indicate the locations of points 'A', 'B' and 'C', at which results are plotted. Another thermocouple (not shown) is located at the same position as point 'A'. (For interpretation of the references to colour in this figure caption, the reader is referred to the electronic version of this article.)

### 7.3. Processing of thermocouple data

The captured thermocouple signals contained sporadic periods of noise caused by the antenna RF field. Processing of these thermocouple signals was required to obtain useful input data for the inverse heat transfer analysis. Spurious short-duration spikes in temperature were present in several thermocouple signals. These spikes were easily identifiable, in many cases having the duration of a single DAQ sample, with temperature value several degrees, or several tens of degrees, different from the preceding and following samples. The spurious temperature values were replaced by linear interpolation of adjacent DAQ samples. Some thermocouple signals contained noise of significant duration that linear interpolation between adjacent DAQ samples was inappropriate. For these signals, the portion of the signal affected by noise was replaced with an interpolating curve fit to adjacent samples.

In order to use the measured temperature data in the inverse model the thermocouple measurements were spatially interpolated and then sampled at the grid node locations of the finite difference grid.

## 8. Experiment heat flux results

Detailed results are presented for experiment 1. A summary of the results of the DOE analysis is then presented.

### 8.1. Experiment 1 results

For experiment 1 the helicon RF power was 1100 W, the electrical current to magnet M1 was 800 A, and the argon propellant mass flowrate was  $2.77 \text{ mg s}^{-1}$ .

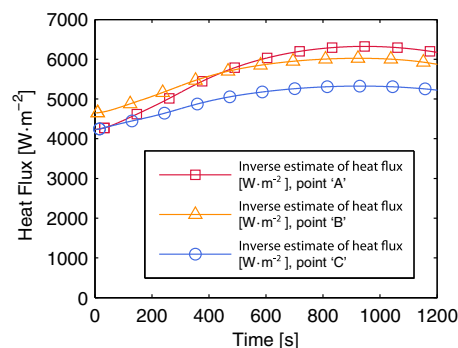
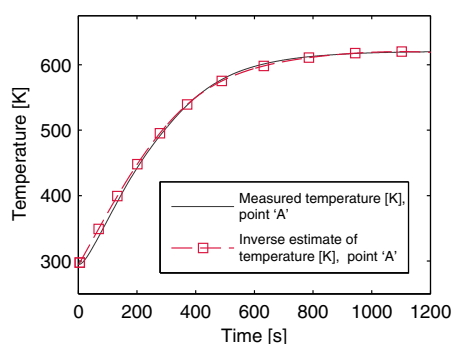


**Fig. 8.** Measured and estimated temperatures at point 'A' on surface  $A_0$  for experiment 1 (left), and heat flux estimates for points 'A', 'B' and 'C' on surface  $A_1$  for experiment 1 (right).

The measured and estimated temperatures at point 'A' on surface  $A_0$ , and the heat flux estimates for points 'A', 'B' and 'C' on surface  $A_1$  are plotted in Fig. 8. The temperature estimate is poorest for the initial 300 s of the experiment. The estimated heat fluxes at the three points considered show a slight temporal variation.

The peak and mean heat flux as a function of time, and the calculated total thermal power flow radially through surface  $A_1$  as a function of time, are plotted in Fig. 9. The temporal variation of the peak and mean heat flux, and the total thermal power, are very similar in character to the temporal variation of heat flux at the three studied sample points (Fig. 8).

The calculated time-averaged spatial variation of heat flux on the surface  $A_1$  for experiment 1 is shown in Fig. 10. The heat flux is highest near the axial centre of the tube, and lower towards each end. The spatial gradient of heat flux in the central portion of the tube is large, with one definite location of peak heat flux occurring.

### 8.2. Variation of RF power

From the DOE matrix of tests, the effect of varying the RF power was studied. The mean heat flux calculated for each test is plotted in Fig. 11 as a function of applied RF power. A strong variation in mean heat flux is observed with varying RF power input. The relationship is approximately linear over the limited range of RF power variation studied. A linear relation was also found by Mulcahy et al. [25] between peak waste heat flux and RF power input, for experiments performed on the VASIMR<sup>®</sup> VX-50 prototype engine.

As the magnet current and gas flowrate were held constant, and the applied RF power increased, the spatial distribution and location of peak heat flux remained broadly unchanged. This result suggests that the RF power does not have a significant effect on the spatial distribution of waste heat—only on the magnitude.

The maximum steady-state temperature occurring on the inner surface of the GCT during the current experiments (calculated from the solution of the direct heat conduction problem) is plotted in Fig. 12 as a function of applied RF power. The maximum allowable operating temperature of fused quartz can become a limiting factor for increases in RF power, requiring the use of a different GCT material such as silicon nitride to operate at higher power levels.

### 8.3. Variation of magnet current

The variation in mean heat flux with current to magnet M1 is plotted in Fig. 13. It is seen that with increasing magnet current the waste heat flux generally decreases. This decrease is slight compared to the variation of waste heat with RF power, over the ranges studied. The reduction in waste heat with increasing magnet current is expected. Higher current to the magnets creates a stronger magnetic field, that results in a more magnetised less collisional plasma, reducing heating of the GCT tube inner surface [6]. The

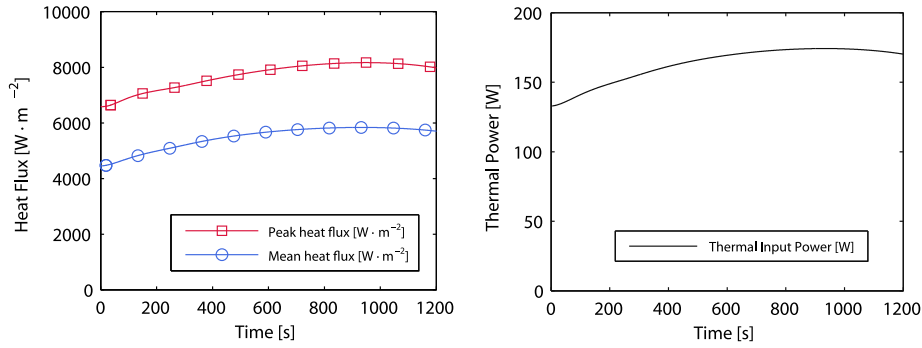


Fig. 9. Peak and mean heat flux on surface  $A_1$  for experiment 1 (left), and total thermal power flow radially through surface  $A_0$  for experiment 1 (right).

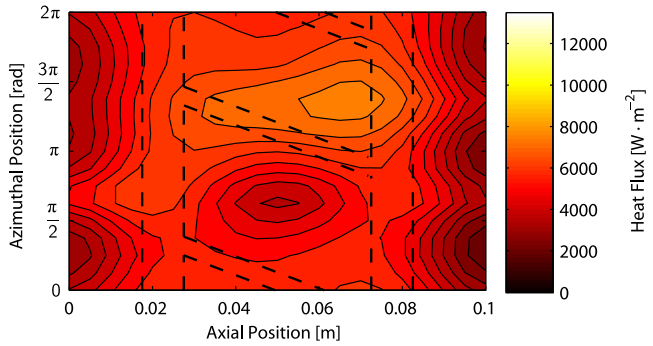


Fig. 10. Calculated time-averaged heat flux on surface  $A_1$  for experiment 1. Dashed lines indicate the antenna strap locations.

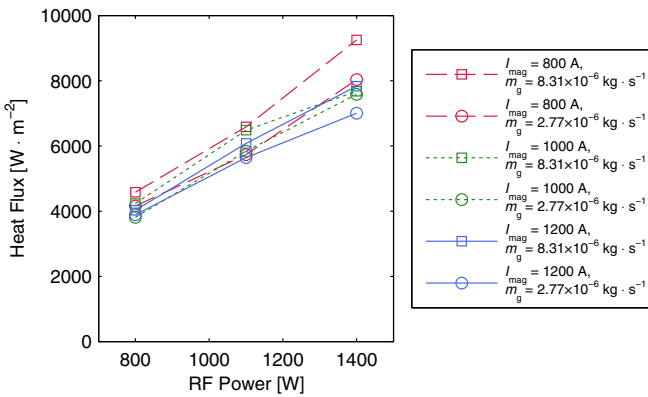


Fig. 11. Mean heat flux as a function of applied RF power, for various currents to magnet M1 ( $I_{mag}$ ) and propellant gas flowrates ( $\dot{m}_g$ ).

relationship between waste heat flux and magnet current is approximately linear over the limited range of magnet current variation studied.

#### 8.4. Variation of propellant mass flowrate

Increasing the propellant mass flowrate from  $2.77 \text{ mg s}^{-1}$  to  $8.31 \text{ mg s}^{-1}$  led to an increase in waste heat flux, as may be observed in Fig. 13. This increased heat flux may be due to a decrease in ionisation rate (ratio of ions in the plasma to the total number of particles) at higher propellant mass flowrates. Neutral particles can collide with ionised particles and absorb energy through a process called *charge exchange*. The resulting high energy neutral particles, which are not contained by the magnetic field,

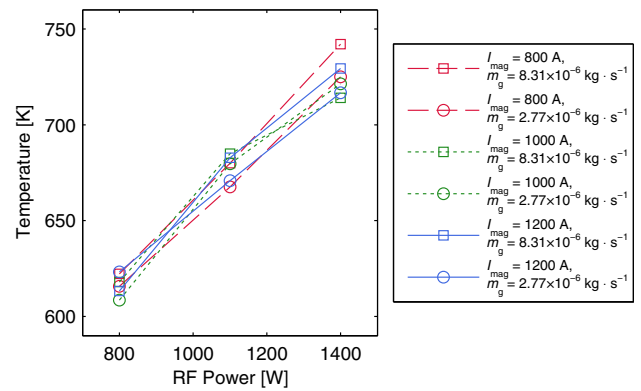


Fig. 12. Peak GCT inner steady-state temperature as a function of applied RF power, for various currents to magnet M1 ( $I_{mag}$ ) and propellant gas flowrates ( $\dot{m}_g$ ).

can impact the inner surface of the GCT, imparting energy to it and thereby increasing the waste heat flux.

#### 8.5. Multiple linear regression analysis

A multiple linear regression analysis was performed on the inverse analysis results. By fitting all of the experimental data from the DOE matrix of tests 3-parameter functions were derived for the mean and peak heat flux as a function of the 3 controlled parameters:

$$q_m = (6.16P_{RF} - 1.42I_{mag} + 101 \times 10^6 \dot{m}_g) \quad (19)$$

$$q_p = (9.17P_{RF} - 0.88I_{mag} + 36.8 \times 10^6 \dot{m}_g) \quad (20)$$

Here  $P_{RF}$  is the RF power (W),  $I_{mag}$  is the current to magnet M1 (A), and  $\dot{m}_g$  is the gas mass flowrate ( $\text{kg s}^{-1}$ ). Expressions of this type are useful for the design of the thermal management system for the helicon section, and also as an input to active cooling system control algorithms.

#### 8.6. Temporal variation of heat flux

For all of the experiments the magnitude of the waste heat flux varied by only a small amount with time. This is to be expected, as none of the controlled parameters (RF power, magnet current, gas flowrate) were varied during each experiment. The time constant of any changes in plasma parameters is also significantly shorter than the thermal time-constant of the tube. For thermal modelling purposes, it may therefore be assumed that the initiation of a plasma shot results in a step change in waste heat flux.

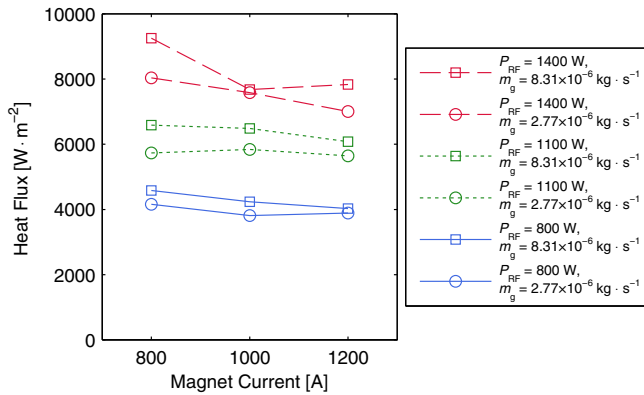


Fig. 13. Mean heat flux as a function of current to magnet M1, for various RF powers ( $P_{RF}$ ) and propellant gas flowrates ( $\dot{m}_g$ ).

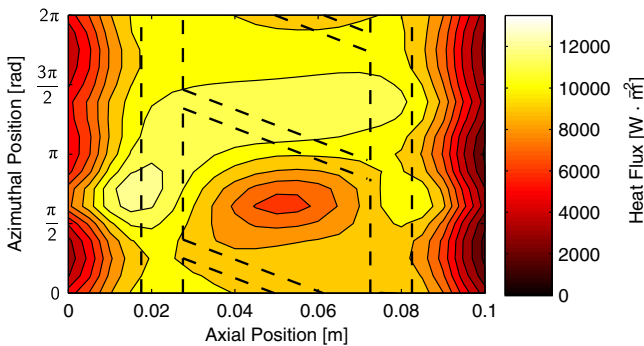


Fig. 14. Calculated time-averaged heat flux on surface  $A_1$  for experiment 10 ( $P_{RF} = 1400$  W,  $I_{mag} = 800$  A,  $\dot{m}_g = 8.31$  mg s<sup>-1</sup>). Dashed lines indicate the antenna strap locations.

### 8.7. Spatial variation of heat flux

The cooling requirement is highest at the locations of peak heat flux. It is therefore important to determine where the locations of highest heat flux are, and how variable they are. The calculated time-averaged heat flux spatial distribution for experiment 1 is shown in Fig. 10. The spatial variation of heat flux is significant. The heat flux is highest under the antenna, and decreases towards each axial end. The high heat flux areas close to the helicon antenna may result from capacitive coupling between the plasma and antenna. For experiment 1 the location of peak heat flux occurred at  $z = 65$  mm,  $\theta = 11\pi/8$  rad. It is possible that locations of higher heat flux exist, but that these are not observed due to the low spatial density of thermocouple measurements.

Varying the controlled parameters did not greatly affect the spatial distribution of heat flux on the inner surface of the GCT. For 16 of the 18 experiments the location of peak heat flux occurred at  $60 \text{ mm} \leq z \leq 70 \text{ mm}$ ,  $\theta = 11\pi/8$  rad. For experiment 9 ( $P_{RF} = 1400$  W,  $I_{mag} = 1000$  A,  $\dot{m}_g = 8.31$  mg s<sup>-1</sup>) the peak value occurred at  $z = 40$  mm,  $\theta = 11\pi/8$  rad. Experiment 10 ( $P_{RF} = 1400$  W,  $I_{mag} = 800$  A,  $\dot{m}_g = 8.31$  mg s<sup>-1</sup>) was the only experiment with a significantly different location of peak heat flux, which occurred at  $z = 15$  mm,  $\theta = 3\pi/4$  rad. The spatial distribution of heat flux for experiment 10 is shown in Fig. 14. The limited measured variation in spatial distribution of heat flux may be in part due to the low spatial resolution of temperature measurements.

### 8.8. Normalised heat flux profile

The spatial distribution of heat flux, normalised using mean-normalisation and peak-normalisation, are plotted in Figs. 15 and 16,

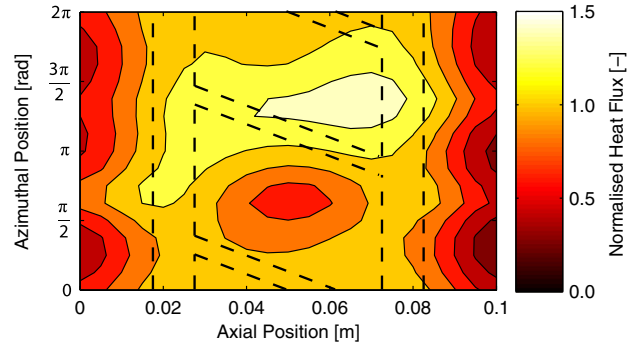


Fig. 15. Mean-normalised heat flux spatial distribution on surface  $A_1$ , averaged over all experiments. Dashed lines indicate the antenna strap locations.

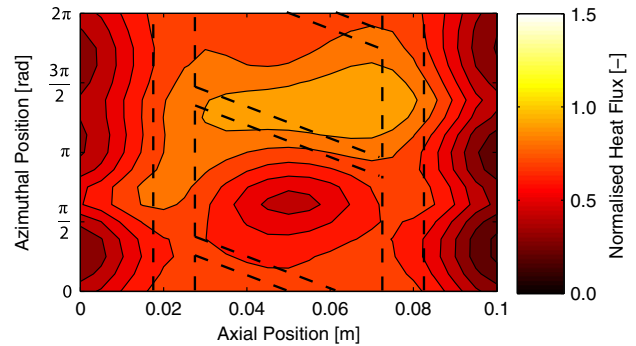


Fig. 16. Peak-normalised heat flux spatial distribution on surface  $A_1$ , averaged over all experiments. Dashed lines indicate the antenna strap locations.

respectively. These normalised heat flux spatial distributions can be used, along with the results of the multiple linear regression analysis to predict the heat flux at any given combination of input parameters.

### 8.9. Axial heat flux profile

The mean-normalised and peak-normalised azimuthally-averaged axial heat flux profiles, averaged over all 18 experiments have been calculated and are plotted in Fig. 17. These data are useful for 2-D (e.g. axisymmetric) thermal modelling of cooling system designs for the VASIMR<sup>®</sup> VX-CR helicon section. These data indicate clearly that the highest heat fluxes occur under the helicon antenna.

## 9. Discussion and conclusions

### 9.1. Comparison with other experiments

The waste heat flux in the plasma discharge tube of the VASIMR<sup>®</sup> VX-50 prototype engine was studied by Mulcahy et al. [25]. There were various differences between the experiments of Mulcahy et al. and the currently described experiments. The geometry and hardware construction of the VX-CR and VX-50 helicon sections are substantially different. Rather than being composed of a discrete endplate, GCT and choke, the VX-50 used a long GCT, which extended past the electromagnets in both the upstream and downstream directions. For the experiments with the VX-50 the RF input power was higher than for the VX-CR experiments. However, due to the limitations of the cooling system for the GCT and cryo-magnets of the VX-50 at that time, plasma shots could only be run for 5 s durations.

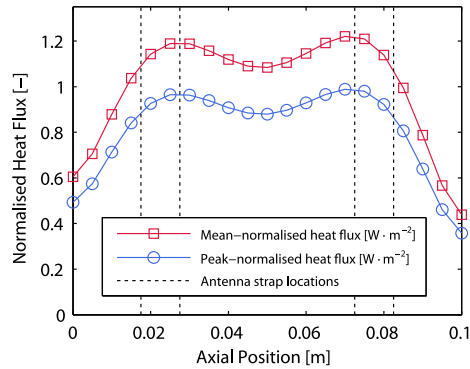


Fig. 17. Mean-normalised and peak-normalised azimuthally-averaged axial heat flux profile.

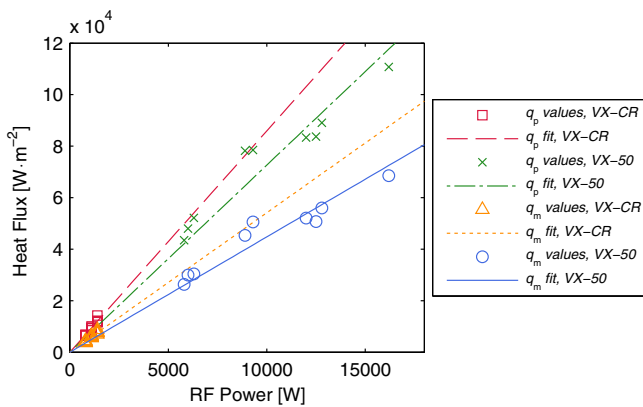


Fig. 18. Mean and peak heat flux for the VASIMR® VX-CR from the current work, and for the VASIMR® VX-50 from Mulcahy et al. [25].

Mulcahy et al. studied the total heat flux on the VX-50 GCT as a function of controlled parameters. The parameters varied were the applied RF power to the helicon antenna (5.8 kW to 16.2 kW), propellant flowrate, and electrical current to the magnets. The study found that both the total heat load and the peak heat flux on the inner surface of the GCT varied approximately linearly with applied RF power, with the current to the magnets and the gas flowrate being held constant. This result was confirmed by the current work over the range of studied RF power variation.

For the VX-50, the waste heat load was  $\approx 39.5\%$  of the input RF power. For the current experiments, the average heat load was 16.2% of the applied RF power, which is significantly lower. However, as the length of the VX-50 tube section studied ( $L = 300$  mm) was significantly greater than that of the tube section studied in the current work ( $L = 100$  mm), it is not possible to directly compare the fraction of input RF power converted to waste heat. Rather, a comparison of the heat fluxes is more appropriate.

The mean and peak heat flux for each experiment of the current study, and each of the experiments of Mulcahy et al., are plotted in Fig. 18 as a function of RF power input. A linear regression fit to the data for the VX-50, assuming zero intercept (as the heat flux is necessarily zero when the power input is zero), yields the functions  $q_m = (4.48 \text{ m}^{-2})P_{RF}$  and  $q_p = (7.26 \text{ m}^{-2})P_{RF}$ . Here  $q_m$  and  $q_p$  are the mean and peak heat flux, respectively. The results of the current study are broadly comparable, yielding the functions  $q_m = (5.41 \text{ m}^{-2})P_{RF}$  and  $q_p = (8.58 \text{ m}^{-2})P_{RF}$ . Given the small range over which the RF power was varied in the current experiments, the regression fits to these data must be treated cautiously.

However, they do support the conclusions of Mulcahy et al. that the peak heat flux varies linearly with applied RF power over the studied range of RF power variation.

## 9.2. Conclusions

The Alifanov iterative regularisation method using a radiation boundary condition, has been shown to successfully recover the net heat flux on the inner surface of a plasma discharge tube.

Thermal steady-state conditions were reached during these experiments. The thermal radiation boundary condition used in this work facilitates the accurate estimation of the heat flux to steady-state conditions, as the method is applicable to high temperatures.

The peak heat flux and total waste heat load from the VASIMR® helicon section scale approximately linearly with RF power, over the range of power inputs tested. The RF input power does not significantly affect the spatial distribution of waste heat flux; only the magnitude of heat flux. The ratio of waste heat flux to applied RF power for the VASIMR® VX-CR engine was found to be broadly similar to that reported by Mulcahy et al. [25] for the VASIMR® VX-50 engine. The spatial distribution of waste heat flux on the inner surface of the GCT was found to be non-uniform. The heat flux is higher in the area directly under the helicon antenna than farther upstream or downstream.

An overall peak heat flux of  $14.3 \times 10^3 \text{ W m}^{-2}$  was calculated for an RF power input of 1400 W. Construction of a cooling system for the helicon section to operate at higher RF power and heat flux levels presents a non-trivial challenge, given that only electrically insulating materials may be used near the helicon antenna.

## Conflict of interest

None declared.

## Acknowledgements

The authors would like to acknowledge the financial support of the FÁS Science Challenge Programme, Ireland, and would like to thank Mr. John Cahill of FÁS, for setting up the collaboration between the Ad Astra Rocket Company and University College Dublin.

## References

- [1] F.R. Chang-Díaz, J.P. Squire, R.D. Bengtson, B.N. Breizman, F.W. Baity, M.D. Carter, The physics and engineering of the VASIMR engine, in: 36th AIAA/ASME/SAE/ASEE Joint Propulsion Conference, Huntsville, Alabama, USA, 17–19 Jul. 2000, <http://dx.doi.org/10.2514/6.2000-3756>.
- [2] E.A. Bering III, B.W. Longmier, C.S. Olsen, L.D. Cassidy, J.P. Squire, F.R. Chang-Díaz, VASIMR®: Deep space transportation for the 21st century, in: AIAA SPACE 2011 Conference & Exposition, Long Beach, California, USA, 27–29 Sep. 2011, <http://dx.doi.org/10.2514/6.2011-7247>.
- [3] J.P. Squire, F.R. Chang-Díaz, T.W. Glover, V.T. Jacobson, G.E. McCaskill, D.S. Winter, F.W. Baity, M.D. Carter, R.H. Goulding, High power light gas helicon plasma source for VASIMR, Thin Solid Films 506–507 (2006) 579–582, <http://dx.doi.org/10.1016/j.tsf.2005.08.061>.
- [4] E.A. Bering, F.R. Chang-Díaz, J.P. Squire, M. Brukaradt, T.W. Glover, R.D. Bengtson, V.T. Jacobson, G.E. McCaskill, L. Cassidy, Electromagnetic ion cyclotron resonance heating in the VASIMR, Adv. Space Res. 42 (1) (2008) 192–205, <http://dx.doi.org/10.1016/j.asr.2007.09.034>.
- [5] A.V. Arefiev, B.N. Breizman, Magnetohydrodynamic scenario of plasma detachment in a magnetic nozzle, Phys. Plasmas 12 (2005) 043504, <http://dx.doi.org/10.1063/1.1875632>.
- [6] D.F. Berisford, R.D. Bengtson, L.L. Raja, Power balance and wall erosion measurements in a helicon plasma, Phys. Plasmas 17 (2010) 033503, <http://dx.doi.org/10.1063/1.3304184>.
- [7] J.I. Del Valle Gamboa, S. Cortés Godoy, L.D. Fonseca Flores, J. Oguilve-Araya, J.J. Valverde Quirós, C. Martínez Castillo, D. Ixcamparij Rojas, R. Chang-Díaz, B.W. Longmier, T.W. Glover, J.P. Squire, F.R. Chang-Díaz, The VX-CR experiment: a thermal and lifetime testbed for the VASIMR® engine, in: 32nd International Electric Propulsion Conference, Wiesbaden, Germany, 11–15 Sep. 2011.

- [8] J.A. Castro Nieto, J. Del Valle, C. Martínez, A. Rivera, J. Oguilve, C.S. Olsen, M. Giambusso, M.D. Carter, J.P. Squire, F.R. Chang Díaz, VASIMR® VX-CR experiment: status, diagnostics and plasma plume characterization, in: 33rd International Electric Propulsion Conference, Washington, DC, USA, 6–10 Oct. 2013.
- [9] M.N. Özışık, H.R.B. Orlande, *Inverse Heat Transfer: Fundamentals and Applications*, Taylor & Francis, New York, 2000.
- [10] C.H. Huang, W.L. Chang, An inverse problem in estimating the volumetric heat generation for a three-dimensional encapsulated chip, *J. Electron. Packag.* 132 (1) (2010) 011004, <http://dx.doi.org/10.1115/1.4000720>.
- [11] S. Beddiaf, L. Perez, L. Autrique, J.C. Jolly, Simultaneous determination of time-varying strength and location of a heating source in a three-dimensional domain, *Inverse Prob. Sci. Eng.* 22 (1) (2014) 166–183, <http://dx.doi.org/10.1080/17415977.2013.828054>.
- [12] W.L. Chen, H.M. Chou, Y.C. Yang, An inverse problem in estimating the space-dependent thermal conductivity of a functionally graded hollow cylinder, *Compos. Part B: Eng.* 50 (2013) 112–119, <http://dx.doi.org/10.1016/j.compositesb.2013.02.010>.
- [13] A.N. Tikhonov, V.V. Stepanov, A.G. Yagola, *Numerical Methods for the Solution of Ill-Posed Problems*, Kluwer Academic Publishers, Dordrecht, Netherlands, 1995.
- [14] K. Levenberg, A method for the solution of certain non-linear problems in least squares, *Q. Appl. Math.* 2 (1944) 164–168.
- [15] D.W. Marquardt, An algorithm for least-squares estimation of nonlinear parameters, *J. Soc. Ind. Appl. Math.* 11 (2) (1963) 431–441.
- [16] J. Beck, B. Litkouhi, C.R. St. Clair Jr., Efficient sequential solution of the nonlinear inverse heat conduction problem, *Numer. Heat Transfer* 5 (3) (1982) 275–286, <http://dx.doi.org/10.1080/10407788208913448>.
- [17] J.V. Beck, B. Blackwell, C.R. St. Clair Jr., *Inverse Heat Conduction: Ill-Posed Problems*, Wiley-Interscience, New York, 1985.
- [18] O.M. Alifanov, *Inverse Heat Transfer Problems*, Springer-Verlag, Berlin, 1994.
- [19] O.M. Alifanov, E.A. Artyukhin, S.V. Rumyantsev, *Extreme Methods for Solving Ill-Posed Problems with Applications to Inverse Heat Transfer Problems*, Begell House, Inc., New York, 1995.
- [20] Y. Jarny, M.N. Özışık, J.P. Bardon, A general optimization method using adjoint equation for solving multidimensional inverse heat conduction, *Int. J. Heat Mass Transfer* 34 (11) (1991) 2911–2919, [http://dx.doi.org/10.1016/0017-9310\(91\)90251-9](http://dx.doi.org/10.1016/0017-9310(91)90251-9).
- [21] C.H. Huang, S.P. Wang, A three-dimensional inverse heat conduction problem in estimating surface heat flux by conjugate gradient method, *Int. J. Heat Mass Transfer* 42 (18) (1999) 3387–3403, [http://dx.doi.org/10.1016/S0017-9310\(99\)00020-4](http://dx.doi.org/10.1016/S0017-9310(99)00020-4).
- [22] C.H. Huang, H.C. Lo, A three-dimensional inverse problem in estimating the internal heat flux of housing for high speed motors, *Appl. Therm. Eng.* 26 (14–15) (2006) 1515–1529, <http://dx.doi.org/10.1016/j.applthermaleng.2005.12.009>.
- [23] C.H. Huang, U.C. Jan, R. Li, A.J. Shih, A three-dimensional inverse problem in estimating the applied heat flux of a titanium drilling - Theoretical and experimental studies, *Int. J. Heat Mass Transfer* 50 (17–18) (2007) 3265–3277, <http://dx.doi.org/10.1016/j.ijheatmasstransfer.2007.01.031>.
- [24] W.L. Chen, Y.C. Yang, H.L. Lee, Three-dimensional pipe fouling layer estimation by using conjugate gradient inverse method, *Numer. Heat Transfer, Part A: Appl.* 55 (9) (2009) 845–865, <http://dx.doi.org/10.1080/10407780902864722>.
- [25] J.M. Mulcahy, D.J. Browne, K.T. Stanton, F.R. Chang-Díaz, L.D. Cassady, D.F. Berisford, R.D. Bengtson, Heat flux estimation of a plasma rocket helicon source by solution of the inverse heat conduction problem, *Int. J. Heat Mass Transfer* 52 (9–10) (2009) 2343–2357, <http://dx.doi.org/10.1016/j.ijheatmasstransfer.2008.10.031>.
- [26] T. Loulou, E.P. Scott, Estimation of 3-dimensional heat flux from surface temperature measurements using an iterative regularization method, *Heat Mass Transfer* 39 (5–6) (2003) 435–443, <http://dx.doi.org/10.1007/s00231-002-0297-8>.
- [27] O.V. Ogorodnikova, About the validity of analytical approximations for temperature and stress for actively cooled windows during thermal loading, *J. Nucl. Mater.* 345 (1) (2005) 41–45, <http://dx.doi.org/10.1016/j.jnucmat.2005.04.067>.
- [28] F.P. Incropera, D.P. DeWitt, T.L. Bergman, A.S. Lavine, *Fundamentals of Heat and Mass Transfer*, sixth ed., John Wiley & Sons, Inc., 2006.
- [29] C. Le Niliot, The boundary element method for the time varying strength estimation of point heat sources: application to a two-dimensional diffusion system, *Numer. Heat Transfer, Part B: Fundam.* 33 (3) (1998) 301–321, <http://dx.doi.org/10.1080/10407799808915035>.
- [30] F. Lefèvre, C. Le Niliot, Multiple transient point heat sources identification in heat diffusion: application to experimental 2D problems, *Int. J. Heat Mass Transfer* 45 (9) (2002) 1951–1964, [http://dx.doi.org/10.1016/S0017-9310\(01\)00299-X](http://dx.doi.org/10.1016/S0017-9310(01)00299-X).
- [31] D. de Faoite, D.J. Browne, F.R. Chang-Díaz, K.T. Stanton, A review of the processing, composition, and temperature-dependent mechanical and thermal properties of dielectric technical ceramics, *J. Mater. Sci.* 47 (10) (2012) 4211–4235, <http://dx.doi.org/10.1007/s10853-011-6140-1>.
- [32] D. de Faoite, D.J. Browne, K.T. Stanton, Regression analysis of temperature-dependent mechanical and thermal properties of dielectric technical ceramics, *J. Mater. Sci.* 48 (1) (2013) 451–461, <http://dx.doi.org/10.1007/s10853-012-6759-6>.
- [33] S. Groß, M. Soemers, A. Mhamdi, F. Al Sibai, A. Reusken, W. Marquardt, U. Renz, Identification of boundary heat fluxes in a falling film experiment using high resolution temperature measurements, *Int. J. Heat Mass Transfer* 48 (25–26) (2005) 5549–5562, <http://dx.doi.org/10.1016/j.ijheatmasstransfer.2005.06.030>.
- [34] J. Su, G.F. Hewitt, Inverse heat conduction problem of estimating time-varying heat transfer coefficient, *Numer. Heat Transfer, Part A: Appl.* 45 (8) (2004) 777–789, <http://dx.doi.org/10.1080/1040778049042499>.